Journal of Alloys and Compounds 869 (2021) 159302

Contents lists available at ScienceDirect

Journal of Alloys and Compounds

journal homepage: www.elsevier.com/locate/jalcom

Mechanical mixing of Mg and Zn using high-pressure torsion

Moara M. Castro[a,*], Luciano A. Montoro[b], Augusta Isaac[a], Megumi Kawasaki[c], Roberto B. Figueiredo[a]

[a] Department of Metallurgical and Materials Engineering, Universidade Federal de Minas Gerais, Belo Horizonte, MG 31270-901, Brazil
[b] Department of Chemistry, Universidade Federal de Minas Gerais, Belo Horizonte, MG 31270-901, Brazil
[c] School of Mechanical, Industrial and Manufacturing Engineering, Oregon State University, Corvallis, OR 97331, USA

ARTICLE INFO

Article history:
Received 20 January 2021
Received in revised form 17 February 2021
Accepted 19 February 2021
Available online 23 February 2021

Keywords:
High-pressure torsion
Metal matrix composites
Magnesium
Zinc
Grain boundary segregation

ABSTRACT

High-pressure torsion (HPT) processing has proved to be a powerful tool to consolidate metallic particles and fabricate nanostructured metal-matrix composites with a wide range of compositions. In this study, HPT was used to fabricate different Mg-Zn composites at room temperature, and the evolution of microstructure and mechanical properties were analyzed by x-ray diffraction, scanning and transmission electron microscopy, dynamic hardness and Vickers microhardness tests. The results show that ultrafine-grained microstructures were achieved in all composites compositions. Smaller grain sizes are observed in Mg-rich phases near areas with significant segregations of Zn. The Mg-rich phase appears to retain less deformation than the Zn-rich phase. Bending and vortex phenomena, that are usually reported in microscale for materials mixed by HPT, are observed in nanoscale in this work. There is evidence of the $MgZn_2$ intermetallic phase with a morphology that varies with composition. Higher levels of deformation imposed by HPT leads to an increase in hardening and a decrease in strain-rate sensitivity which are attributed to the tendency to form intermetallics and Zn segregations that prevent grain boundary sliding. Moreover, a model is proposed to explain the mixing of phases in microscale and its relation to the evolution of mechanical properties.

1. Introduction

Severe plastic deformation (SPD) is one of the widely used methods for producing ultrafine-grained structure of metals and alloys which usually results in exceptional mechanical strengthening. SPD processing is also an effective tool to consolidate metallic particles to produce bulk materials. In respect of consolidation, high-pressure torsion (HPT) is the most efficient technique because the processing is generally conducted under a high hydrostatic compressive stresses state and high shearing deformation. These conditions lead to the deformation and bonding of the particles while preventing cracking of the sample, enabling to process a wide range of materials. Many papers have reported the successful consolidation of pure metals [1,2], alloys [3], and even harder materials such as partly amorphous [4] and fully amorphous [5] metallic glasses. Besides, a variety of metal-matrix composites were fabricated by HPT by the mixture of metallic particles and hard inert materials. For example, Al based composites were produced by HPT processing of Al particles mixed with Al_2O_3 [6,7], carbon nanotubes [8], fullerene [9] and Nb_2O_5 [10]. Recent papers also showed successful production of Mg based composites with different reinforcement phases such as Al_2O_3 [11,12], quasicrystal [13] and bioactive materials [14,15]. These composites in which hard phases are incorporated, usually display an increase in strength in the range of Hall-Petch strengthening, as the inert phases enhance the grain refinement during HPT [16].

Moreover, HPT can be used for processing non-inert phases such as metal mixtures, and this provides the opportunity to induce solid state reactions during deformation, enabling the achievement of further improvement in strength and other properties. Examples of such reactions include formation of supersaturated solid solutions [17,18], segregation of alloying elements in crystalline defects [19], and the formation of different phases [20,21]. Hence, there has been an increasing interest in HPT of different metallic materials combined, either by consolidating a mixture of metal powders, machining chips, or by stacking different discs together. Many different systems have been processed including Al-Mg [22–28], Al-Cu [29], Ag-Ni [30], Cu-Ag [31–33], Cu-Co [34–37], Cu-Zr [38], Cu-Cr [18,39], Cu-W [40–42], Cu-Ta [43], Fe-Cu [17,38,44,45], Fe-V [38,46], Fe-Zr [38], V-Zr [38,45,47], Zr-Nb [48], and Zn-Mg [49–51].

Among those systems, magnesium and zinc alloys are of great interest due to their high potential for biological applications since both are biocompatible and biodegradable materials which could be

---

[*] Corresponding author.
E-mail address: m-castro@ufmg.br (M.M. Castro).

https://doi.org/10.1016/j.jallcom.2021.159302
0925-8388/

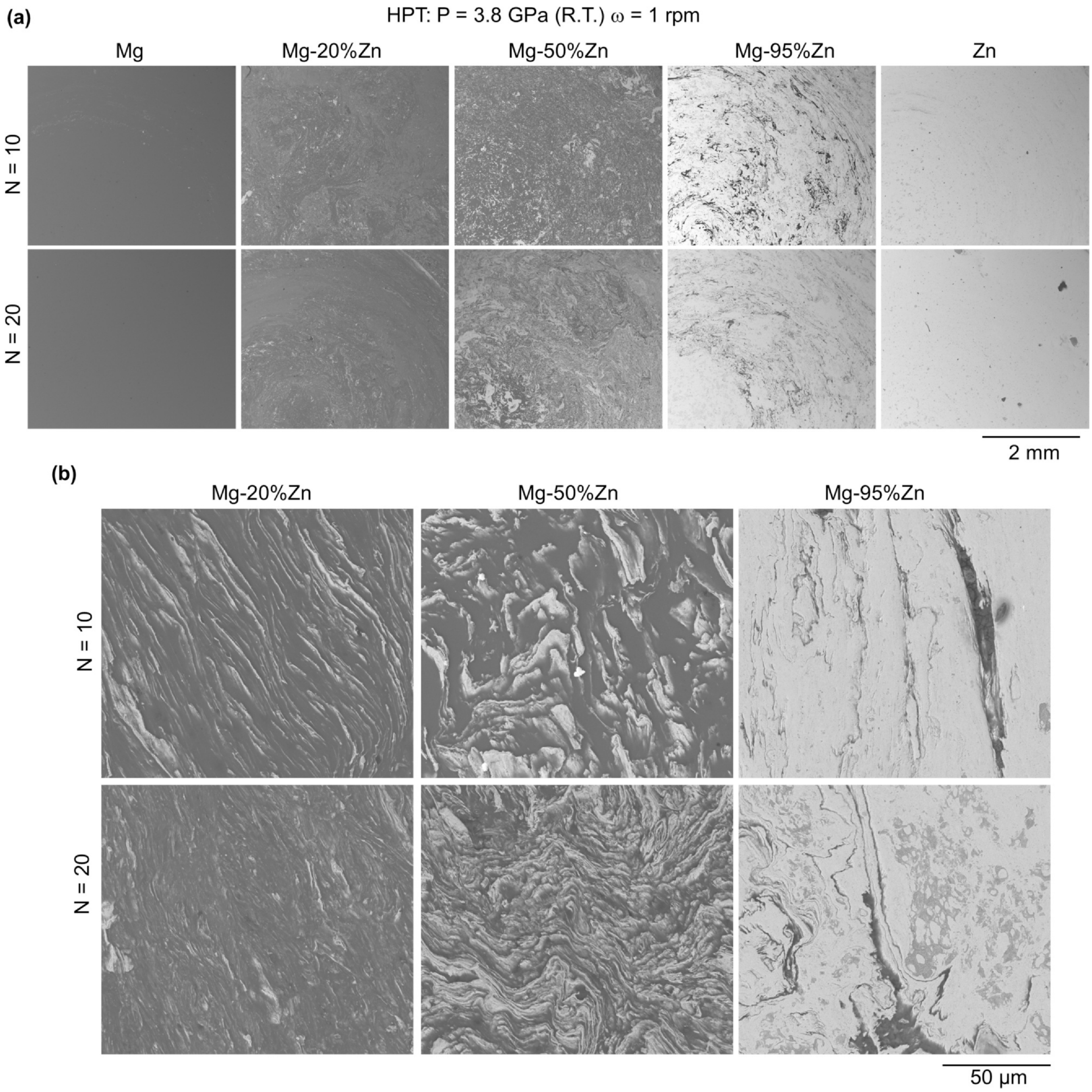

Fig. 1. BSE-SEM images of the Mg-Zn composites after 10 and 20 HPT turns: (a) general surface of all samples, and (b) surface at mid-radius of the Mg-Zn composites.

used to produce temporary implants. Recent papers have shown that HPT processing does not affect the biocompatibility of Zn and Mg [52] and might even improve Mg corrosion resistance [53–55]. Although recrystallization and grain growth take place in pure Zn after HPT limiting the strengthening in this material [56], alloying with Mg usually leads to finer grain sizes and higher strength [52,57,58]. The main strengthening mechanism of the Zn-Mg system has been attributed to the Hall-Petch effect and precipitation of intermetallics [51]. Also, experiments with bulk Zn-Mg alloys have showed that grain growth is prevented and ultrafine grains are developed by hydrostatic extrusion [59]. In this study, a wide range of composition of Mg-Zn composites were synthesized by mechanical alloying of the elemental powders using HPT at room temperature. The microstructure and mechanical properties of the HPT-processed composites were systematically investigated. Special attention was given to the effect of Zn content on the deformation process and mixing of the different components.

2. Experimental procedure

Magnesium particles with a sizing range of 20–100 μm and zinc powders with 2–10 μm in diameter were used in the present work. Scanning electron microscope (SEM) images of these initial materials are available as Supplementary Material (Fig. S1). The particles were separated into groups of pure magnesium, pure zinc and mixtures of Mg-20 wt% Zn, Mg-50 wt% Zn and Mg-95 wt% Zn. Each group was prepared by hand mixing, cold pressed at 400 MPa and processed by 10 and 20 turns of HPT using a nominal pressure of ~3.8 GPa and rotation speed of ~1 rpm. The discs had an initial

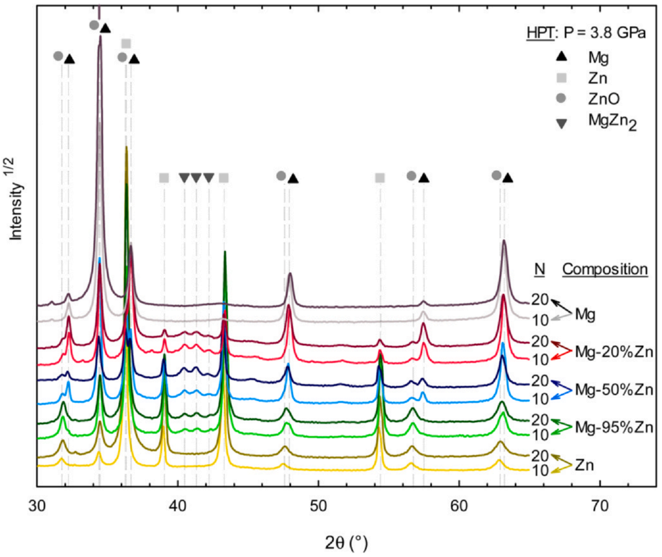

Fig. 2. X-ray diffraction patterns of the different materials.

diameter of 10 mm and thicknesses of ~1 mm. After HPT processing, the thickness of the discs was reduced to ~0.7 mm.

The processed discs were ground and polished using 3 μm and 1 μm diamond paste. Final polishing was carried out using colloidal silica suspension. The polished surfaces were observed using a JEOL 6360LV scanning electron microscope operating at 15 kV. X-ray diffraction was used on the polished surface to determine the major phases present. A Philips PW1710 diffractometer operating with Cu Kα radiation and a graphite monochromatic crystal with a wavelength of 1.5406 Å was used. The step was 0.01° with 2 s of time and the diffraction was collected in the range 30–65°.

Thin lamellae were extracted at ~4 mm from the disc center using focused ion beam milling. The lamellae were observed using a Tecnai G2–20 - SuperTwin FEI - 200 kV transmission electron microscope operated at 200 kV. Images were obtained using transmission (TEM) and scanning transmission electron microscopy (STEM) techniques, with bright-field (BF) and annular dark-field detection (ADF). Particularly, the Mg-20% Zn composite processed to 20 turns was also observed using STEM images on a FEI Titan Themis Cubed (FEI Company) operated at 300 kV, equipped with a Cs probe corrector. High angular annular dark field (HAADF) images were also obtained in order to provide better composition contrast. Local composition mapping was performed by using a Super-X EDS with four windowless silicon-drift detectors. The grain size was estimated by measuring the length of at least 50 different grains in each sample. It was not possible to distinguish the misorientation of grains and therefore subgrain boundaries were also considered grain boundaries.

Vickers microhardness tests were carried out at different locations using a load of 100 gf and 10 s of dwell time. The position of each indentation was recorded in order to determine its distance to the disc center which was used to estimate the effective strain imposed during HPT processing. A minimum of 5 indentations were carried out in locations with reduced scattering of the hardness and up to 20 indentations were carried out in areas with large scattering. Additionally, dynamic hardness tests were carried out at mid-radius locations of the discs using a Shimadzu DUH-211s equipment. A maximum load of 300 mN was applied for up to 999 s and the evolution of penetration depth was tracked with time. Care was taken to maintain constant temperature during these tests. The time and depth were used to estimate the strain rate following procedure reported in the literature [60,61]. The flow stress was estimated as the instant hardness divided by 3 [62] and plots of flow stress vs strain rate were used to estimate the strain-rate sensitivity.

3. Results

3.1. General microstructure

Fig. 1 shows SEM images from backscattered electrons (SEM-BSE) of the surfaces of the processed samples. The observed surfaces are perpendicular to the torsion axis of each sample. In Fig. 1(a), low magnification images of the discs processed to 10 (upper) and 20 turns (lower) of HPT are presented, where the bottom left of each image corresponds to the center of the disc. Because the deformation imposed during HPT is proportional to the distance from the disc center [63], the bottom left of each image corresponds to an area which underwent a lower plastic deformation; and the top right corresponds to an area submitted to larger strain. The image contrast observed in Fig. 1 is related to variations in atomic number of the analyzed region. Thus, pure Zn (right) appears brighter and pure Mg (left) appears darker. Intermediate intensity levels can be also visualized in certain regions of the samples, which indicates the effective mixing of Mg and Zn at finer scales.

Higher magnification images taken at the mid-radius of the composites are presented in Fig. 1(b). The contrast between different areas is clearly observed, thereby indicating that the Mg-rich and Zn-rich phases remain still present in all composites up to 20 turns of HPT. Nevertheless, thicknesses of the phases considerably decrease with increasing number of HPT turns for the Mg-20% Zn and the Mg-50% Zn composites, suggesting a better mixing between the phases. The Mg-95% Zn composite - which is the only one having Zn as the major component - fails to show the occurrence of a greater mixing with increasing the number of HPT to 20 turns. In addition, an alignment between the phases and the shear direction can be observed in many areas of the discs, mostly Mg-20% Zn composite, as well as folding of phases in some areas. Bent phases with curvature radius higher than 1 μm are observed, mostly Mg-50% Zn composite. Both effects of alignment and folding of phases have been reported in literature in multiphase materials processed by HPT [20,38,64,65].

According to SEM investigation, it appears that HPT can fully consolidate pure Mg and Mg-Zn composites in which Mg occupies a larger volume fraction. However, pure Zn and Mg-95% Zn samples after 10 and 20 turns of HPT still exhibit some clear boundaries between original Zn particles, thereby indicating an apparent lack of bonding in these areas. Yet, great majority of their volume were consolidated.

The X-ray diffraction peak profiles are shown in Fig. 2 for the Mg-Zn composites, pure Mg and pure Zn discs after 10 and 20 HPT turns. The detected main constituent phases are Mg, Zn, ZnO, and $MgZn_2$. Zinc oxide peaks are clearly visible in the XRD patterns of all samples produced with Zn, what indicates that ZnO corresponds to a significant portion of the original particles. The presence of some naturally oxidized surface layer is expected on metallic particles. However, MgO peaks were not identified in XRD indicating that the fraction of this phase in the initial Mg particles is reduced. This is attributed to the larger size of the Mg particles and, consequently, reduced surface area prone to oxidation. All three Mg-Zn composites exhibit the peaks related to $MgZn_2$, which confirms the occurrence of phase transformation and intermetallic formation during HPT processing. This agrees with recent observations of intermetallic formation in Zn-Mg composites produced by HPT processing of stacked discs [49–51]. In addition, the intensities of the peaks related to Mg or Zn are higher than the ones related to the other phases identified confirming that the pure metals are the major constituent of the composites.

3.2. Transmission electron microscopy

Transmission electron microscopy (TEM) analyses were carried out for a detailed examination of the microstructure of the Mg-Zn

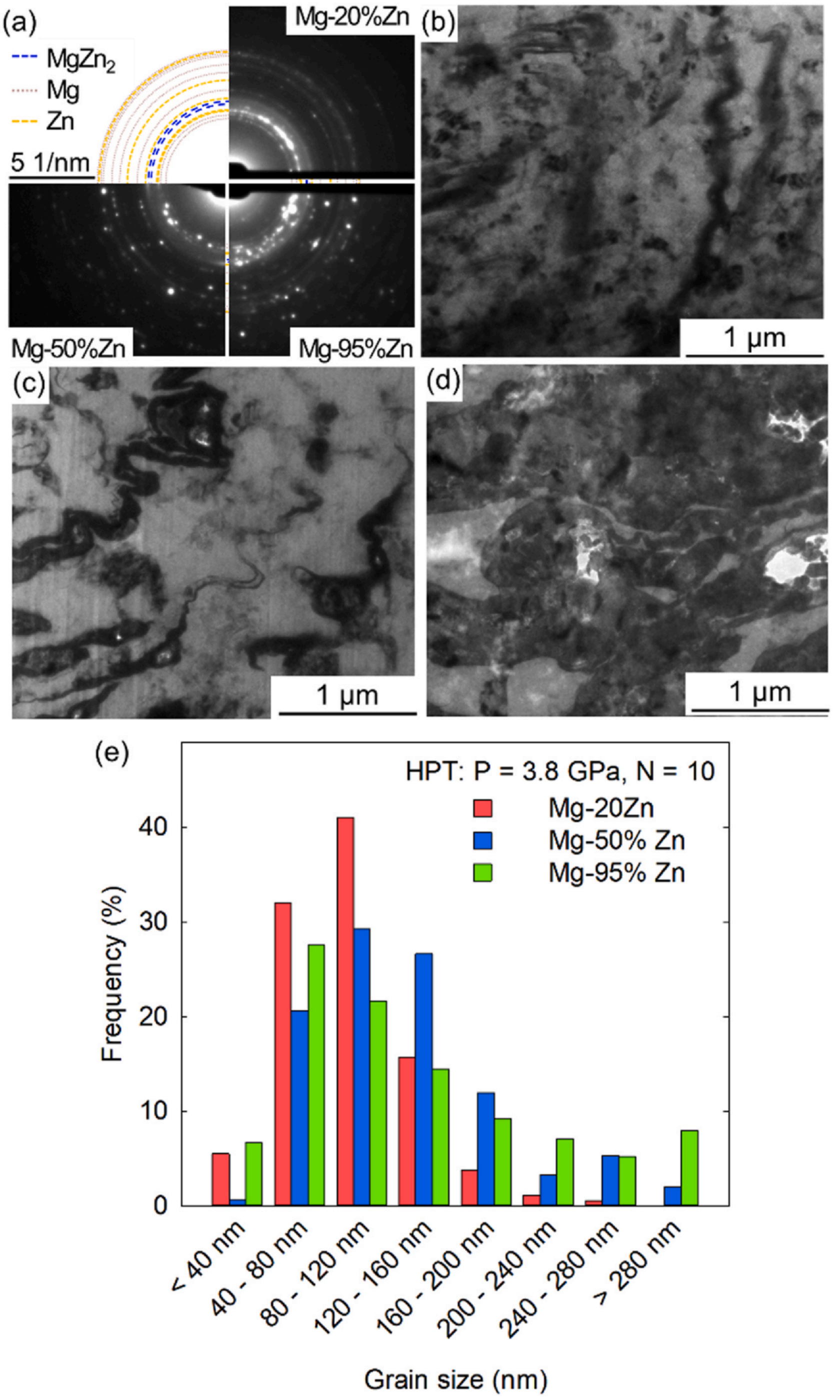

Fig. 3. Mg-Zn composites processed to 10 turns of HPT: (a) SAED patterns of the samples, (b–d) BF-TEM images of: b) Mg-20% Zn, c) Mg-50%Zn, and d) Mg-95% Zn; and (e) grain size distribution.

composites. Fig. 3(a) shows selected area electron diffraction (SAED) patterns of large areas of the lamellae of the three composites processed for 10 turns of HPT. These patterns confirm the presence of three main phases: Mg, Zn, and $MgZn_2$. The higher intensities of the SAED patterns are associated with the pure metals which agrees with the XRD results. Zinc oxide could not be properly distinguished in the patterns. Fig. 3(b)–(d) presents STEM-BF images of the composites from which the patterns displayed in Fig. 3(a) were taken. The Mg-20% Zn (Fig. 3b) and Mg-50% Zn (Fig. 3c) samples exhibit thin (< 100 nm) and elongated areas of Zn in the Mg matrices. Folding of the Zn-rich phase in which the radius of curvature is smaller than 1 µm also visible in these composites. The Mg-95% Zn (Fig. 3d) composite exhibits elongated and folded Mg-rich areas in the Zn matrix. Submicrometer voids (the brightest regions) can be identified in the Mg-95% Zn composite, indicating poorer consolidation when compared to the other two composites.

The grain size distributions of the Mg-Zn composites are presented in the histogram of Fig. 3(e). The composites display a broad range of grain sizes including grains smaller than 40 nm and grains larger than 240 nm. The average grain sizes measured were ~95 nm, ~130 nm, and ~135 nm for the Mg-20% Zn, Mg-50% Zn and Mg-95% Zn composites, respectively. In addition, the SAED patterns also suggest differences in grain sizes. The SAED patterns of Mg-50% Zn and Mg-95% Zn are significantly dotted which is an evidence of

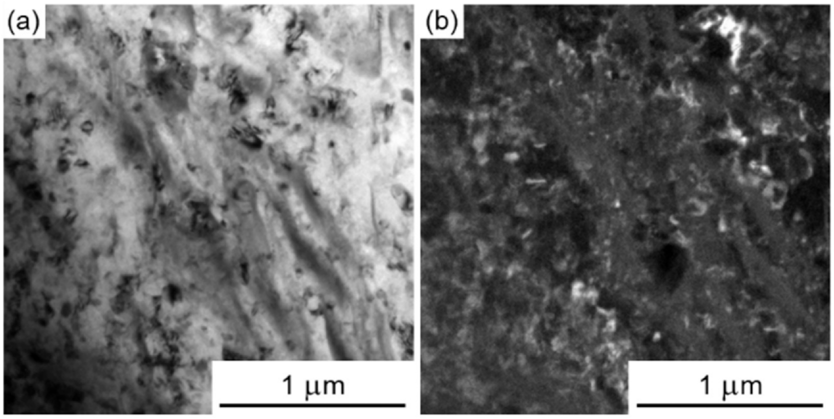

Fig. 4. STEM (a) BF and (b) DF images of the Mg-20% Zn composite processed to 10 turns of HPT.

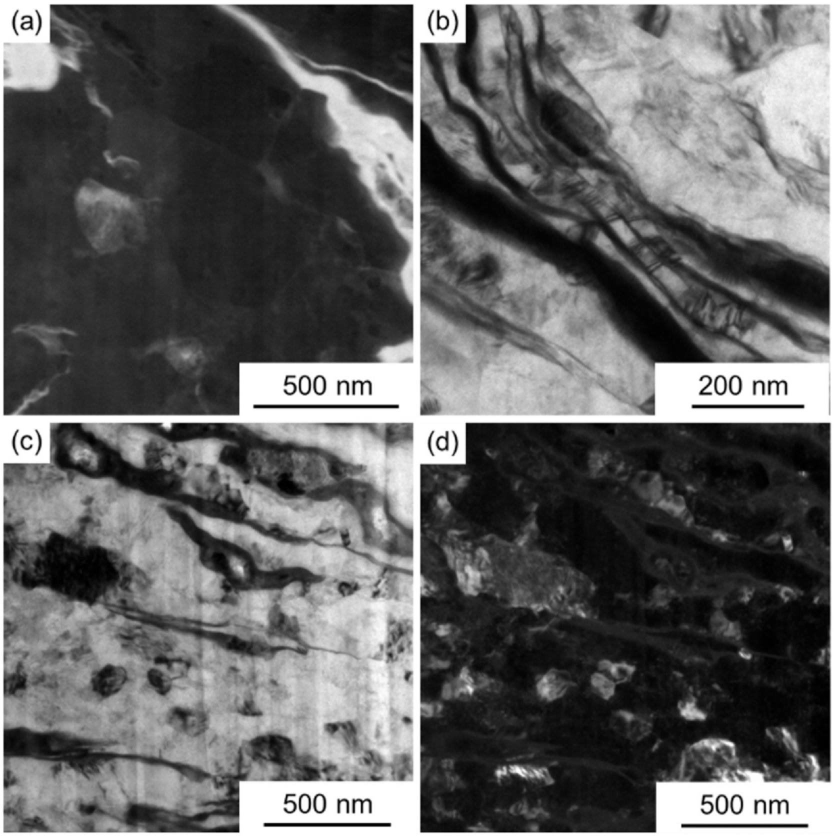

Fig. 5. (a) ADF-STEM, (b) BF, (c) BF, and (d) DF images of the Mg-50% Zn composite processed to 10 turns of HPT.

coarse grains. On the other hand, the Mg-20% Zn pattern shows more uniform and diffuse rings, indicating smaller grains.

The TEM and STEM images shown in Figs. 4–6 provide additional information on the microstructure of the Mg-20% Zn, Mg-50% Zn and Mg-95% Zn composites, respectively. The BF-TEM image of the Mg-20% Zn composite, shown in Fig. 4(a), shows elongated strips with less than 100 nm thickness slightly darker than the matrix. These strips are attributed to Zn-rich areas. The dark-field (DF) TEM image in Fig. 4(b) reveals the presence of several isolated Mg-rich grains (bright) with less than 100 nm.

Fig. 5(a) presents an ADF-STEM image of the Mg-50% Zn composite. It is possible to distinguish Zn-rich areas (bright) dispersed in the Mg matrix. In addition, very thin layers (intermediate gray level) at the Mg grain boundaries can be distinguished which indicate the Zn segregation. Due to the contribution of diffraction effects in BF imaging, Fig. 5(b) clearly shows long and thin strips of Zn (dark). These strips display thicknesses as thin as a few tens of nanometers and appear slightly folded. Fig. 5(c) and (d) shows BF- and DF-TEM images of the same area of the sample and reveal a wide range of grain sizes. The majority of grains observed in this composite have less than 100 nm in length, but some grains of hundreds of nanometers are also present. It is important to note that there was a limitation in the TEM examination to distinguish grains within the Zn-rich areas in both Mg-20% Zn and Mg-50% Zn composites.

Further details of the structural features observed in the Mg-95% Zn composite after 10 turns of HPT are shown in Fig. 6. Areas with fine and distorted grains are distinguishable from some coarser grains with clean interior in the BF-TEM image in Fig. 6(a), suggesting the partial recrystallization of this sample. This agrees with a report of recrystallization and grain growth at room temperature in

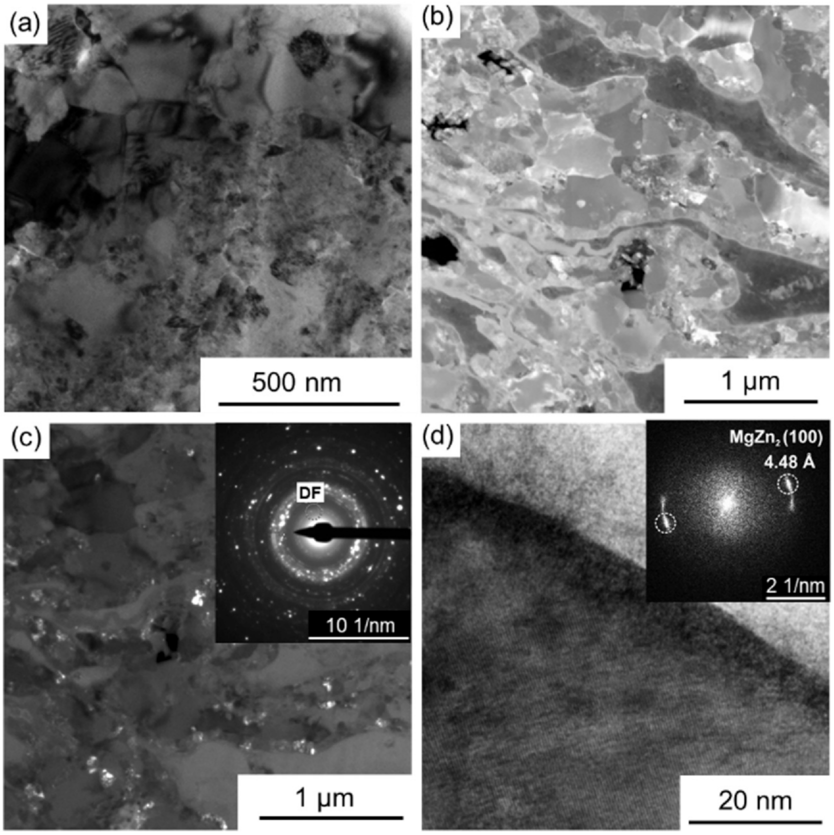

Fig. 6. Images of the Mg-95% Zn composite processed to 10 turns of HPT: (a) BF-STEM, (b) ADF-STEM, (c) DF with the corresponding diffraction pattern, and (d) HRTEM with the corresponding FFT.

zinc processed by HPT [56]. The ADF-STEM image in Fig. 6(b) clearly shows grains with a broad range in sizes. Also, small black areas which correspond to pores can be visualized. These cavities support the idea that the surface oxide layer of the original Zn particle hindered the full consolidation. During the TEM analysis of this sample it was noted the presence of regions with an intermediate gray level at the Mg/Zn interfaces, which suggests the formation of a new phase during HPT processing. The thickness of these layers lies in the range of tens of nanometers. In order to evaluate the presence and distribution of $MgZn_2$ phase, a dark field image was collected from the reflections associated with this phase. The DF-TEM image with the corresponding diffraction pattern, is shown in Fig. 6(c), and reveals the presence of the $MgZn_2$ phase, evidenced by the weak rings and dots corresponding to 4.49 Å (100), 4.26 Å (002), and 3.97 Å (101) lattice spacings (planes). Many of the $MgZn_2$ particles in this image are located in the interface between Mg and Zn phases. Fig. 6(d) shows an HRTEM image in which a lattice spacing of 4.49 Å is visible next to the Mg area (bright phase on the top right). This interplanar spacing is associated with $MgZn_2$ (100) planes.

For comparison purposes, DF-TEM images of the Mg-20% Zn composites processed to 10 and 20 turns of HPT are shown side by side in Fig. 7(a), and the corresponding grain size distributions are presented in Fig. 7(b). It is apparent that significant grain refinement occurred with increasing numbers of turns of HPT. The average grain size decreased from ~95 nm to ~70 nm with the increase from 10 to 20 turns.

Fig. 8 presents additional information on the microstructure of the Mg-20% Zn composite processed to 20 turns of HPT. The HAADF-STEM image, displayed in Fig. 8(a), show that the morphology of the Zn-rich phases (bright) is quite heterogeneous throughout the sample. Fig. 8(b)–(d) correspond to magnified views of the regions indicated by red squares in Fig. 8(a). Fig. 8(b) shows folded regions of Zn, whereas elongated ribbons with thicknesses ranging from few to tens of nanometers are observed in Fig. 8(c) and (d). These findings indicate that areas of the composite distanced few microns apart from each other experienced different shear paths and deformations.

Fig. 8(b) reveals two folded Zn ribbons less than 100 nm apart connected by extremely thin bright lines. These lines indicate the segregation of Zn along Mg boundaries. Fig. 8(c) shows a high magnification image of the region c in Fig. 8(a) and the EDS mapping associated with the region confirms that the bright areas are rich in Zn and the dark matrix is rich in Mg. The images show that Zn-rich veins separate the volumes of Mg as thin as a few tens of nanometers. Fig. 8(d) shows coarse volume of Zn surrounded by Zn fragments. This observation suggests the fragmentation of the initial components during HPT processing. Careful analysis of the HAADF-STEM image in Fig. 8(e) and (f) reveal that the Mg grain size differs significantly in close proximity to the Zn phase. For instance, the Mg grains close to the Zn-rich areas on the bottom Fig. 8(f) are clearly smaller and an extensive segregation of Zn can be observed at the boundaries of these grains. The region of the upper part of Fig. 8(f) displays coarser Mg grains with the presence of the Zn segregations in more than ~100 nm distancing. This indicates that higher levels of Zn segregations can prevent grain growth and reduce the grain size of Mg.

Fig. 9(a) shows a HAADF-STEM image of the Mg-20% Zn composite revealing different Zn-rich areas including some clusters with ~2 nm in size. A high-resolution image of the area marked in red around these particles is shown in Fig. 9(b), in which is possible to distinguish atomic planes in one of them. The respective Fast Fourier Transform (FFT) and a line profile of HAADF intensity are shown in the right side of this image and a spacing of 2.31 Å was determined, which is associated with Zn (100) planes.

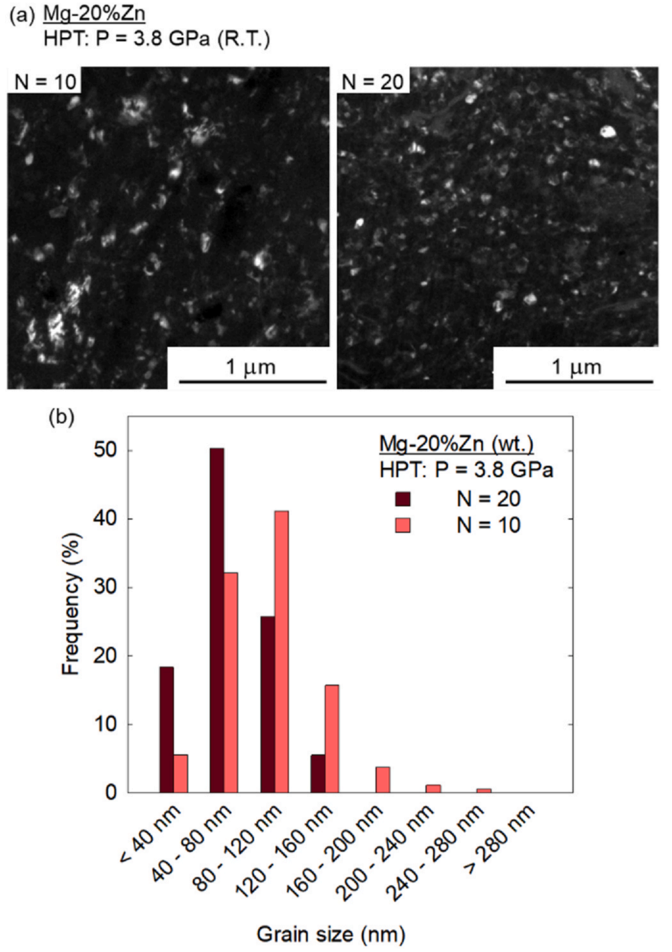

Fig. 7. Mg-20% Zn composites processed to 10 and 20 turns of HPT: (a) DF-TEM images and (b) the grain size distributions.

The formation of $MgZn_2$ in the Mg-20% Zn composite processed to 20 turns of HPT could be confirmed. As it is shown in Fig. 9(c), the precipitates were located preferentially associated to grain boundaries which were decorated by Zn atoms and their sizes were in the range of tens of nanometers. A higher magnification of one of these precipitates which was located at a grain boundary triple junction is shown in Fig. 9(d). The FFT of the high-resolution image reveals atom positions associated with the Mg grains and positions having an interplanar spacing of 4.0 Å which is associated with $MgZn_2$ (101) planes.

3.3. Mechanical properties

Fig. 10 summarizes the mechanical properties of the HPT-processed samples. Fig. 10(a) shows the evolution of microhardness as a function of the effective strain imposed to the materials. The continuous lines serve as guide to the eyes. Pure Zn and pure Mg samples display reasonably constant hardness values at ~45 Hv and ~55 Hv, respectively, with increasing equivalent strain. The lack of hardening agrees fairly well with reports in the literature for bulk Zn [56] and Mg [54,66]. All Mg-Zn composites display higher hardness than the pure metals although a significant scatter in data was observed. This scatter is attributed to the significant changes in microstructure that do not take place homogeneously throughout the sample. It is interesting to note that the composites present a near saturation in hardness at strains of ~100 but a second hardening stage takes place at even higher strains. Such effect, different hardening stages, has been reported in many hybrid materials processed by HPT [67]. At strains > 300, the Mg-50% Zn exhibits the highest hardness among the composites (some measurements give hardness values above 170 HV) while the Mg-95% Zn shows the lowest (hardness values not higher than 120 HV).

Dynamic hardness tests were used to estimate the strain-rate sensitivity, m, of all the HPT-processed materials. Fig. 10(b) shows representative curves of flow stress plotted as a function of the strain-rate and the slopes of these curves can estimate the values of m. The estimated m values are summarized for the materials in Fig. 10(c) where the average microhardness values are indicated by squares and the m values are indicated by circles (determined for strain-rates lower than ~10^{-4} s^{-1}), and are plotted as a function of the Zn content in the composite for the samples processed to 10 and 20 turns. Both, pure Mg and pure Zn display curves with high slope which agrees with reports of high strain-rate sensitivity in pure Mg processed by HPT [61,68] and in pure Zn [69]. The composites also display a high strain-rate sensitivity after processing by 10 turns of HPT only. However, increasing the number of turns in HPT increased their hardness and reduced their strain-rate sensitivity.

4. Discussion

4.1. Mixing of phases and formation of segregations

The present HPT consolidation of dissimilar metal powders is anticipated to introduce continuous and homogeneous shear deformation promoting thinning and alignment of phases along the shear direction. This effect has been observed in many multi-phase materials such as Fe-Cu [17] and Cu-Ag alloys [70], and pearlitic steel [71]. However, it is now known that the homogeneity of deformation during HPT can be affected by processing conditions such as anvil misalignment [72–74] and friction between the anvil and the sample [75]. The presence of different phases can also induce local heterogeneities in deformation and finite element modeling has shown changes of local material velocity, thus plastic instability, due to the presence of phases with different strength [76–80]. The heterogeneity of deformation in HPT can induce variations in hardness along the thickness of samples [81–83] and also develop local vortices of material flow inducing the curving of different phases. Vortex-like patterns have been observed using optical microscopy and SEM in many multi-phase materials [70,78,84,85].

Experiments by stacking of dissimilar metal discs revealed the microstructural evolution with different patterns upon HPT deformation. Continuous thinning of phases occurs due to delamination of individual layers in the early stage of deformation in stacked discs of Ag and Cu while folding of Cu layers takes place in Al and Cu stacked discs [64]. However, after larger deformation both systems develop tangled and turbulent-like patterns indicating pronounced mixing at the nanometer and even atomic scales. These different patterns were successfully predicted using numerical simulations in which the phases were treated as nonlinear viscous fluids with different viscosity ratios [64]. A recent paper [38] also combine different materials (Fe, V, Zr, Cu) using HPT to evaluate the formation of turbulent flow at their interface, and concluded that the structure evolution depends on the hardness ratio between the phases and their deformation capacity. It was shown that significant differences in hardness between the materials lead to smooth interfaces while similar levels of hardness and deformation capacity induce multilayered vortex structure. Thus, when there is a significant difference in hardness between the phases, the softer phase accounts for most of deformation inhibiting deformation of the harder phase and good mixing. Turbulent flow and vortices formation are associated with increased deformation and promotes better mixing of phases.

The present results show evidence of both co-deformation and bending of phases at different length scale in the Mg-20% Zn and Mg-50% Zn composites. In practice, bent phases with curvature

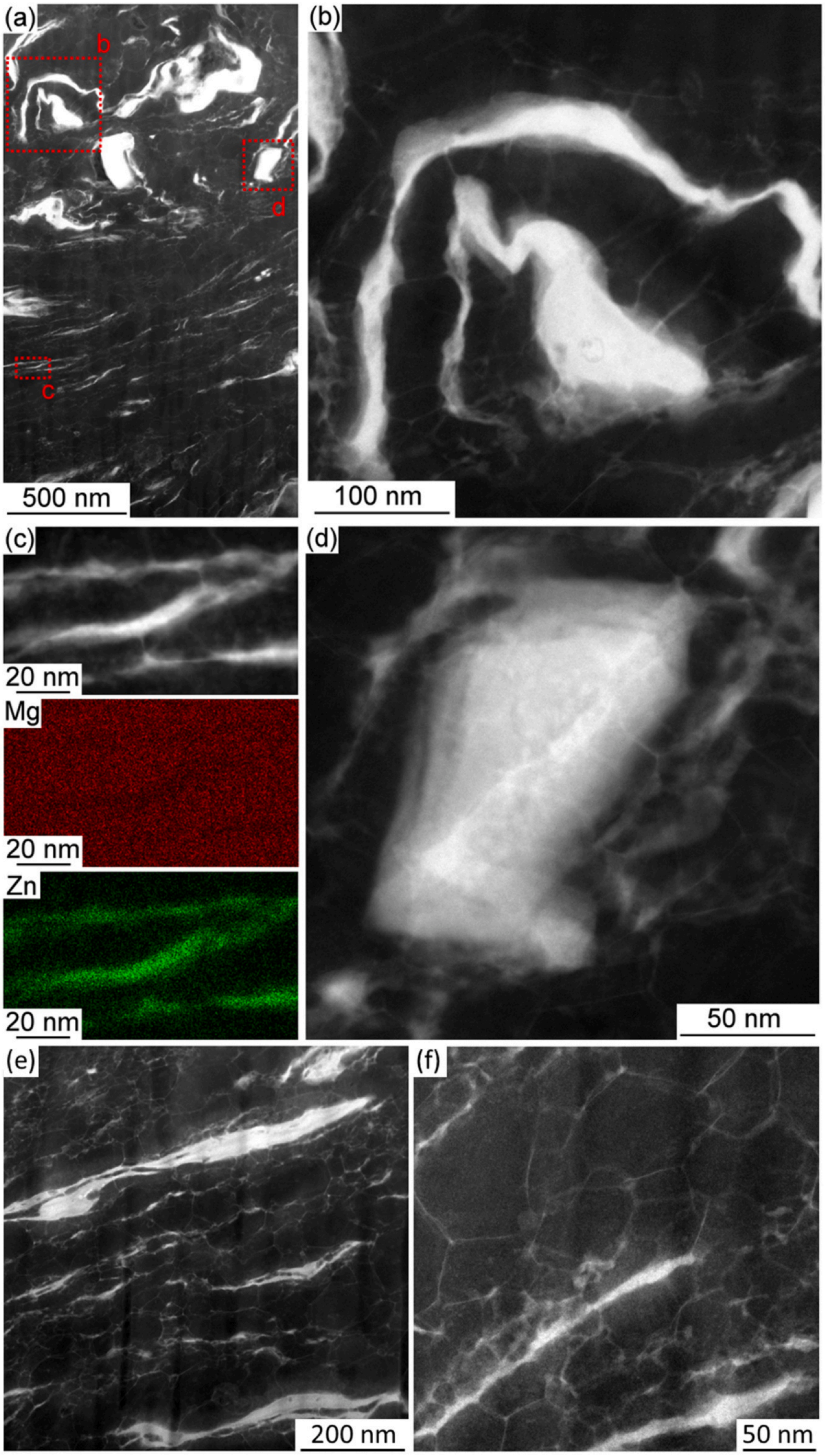

Fig. 8. HAADF-STEM and EDS composition maps of the Mg-20% Zn composite processed to 20 turns of HPT.

radius higher than 1 µm were observed using SEM and bent phases with curvature radius of ~100 nm were observed using TEM/STEM. Thus, the heterogeneity of plastic flow reported for many systems at microscale also takes place at sub-micron scale and contribute to mixing of phases. On the other hand, the Zn-rich Mg-95% Zn composite did not display significant mixing, and Zn and Mg phases appears elongated as shown if Figs. 1(b) and 3(d), suggesting co-deformation. Also, the Mg phase is thicker in this Zn-rich composite than the Zn phase in Mg-rich composites. This suggests that Zn is softer and undergoes larger deformation, which agrees with the slightly lower hardness in pure Zn discs when compared to the values in pure Mg discs. The observation of a thick and continuous layer of $MgZn_2$ intermetallic around the Mg phase also supports the assumption that this phase undergoes less deformation. The plastic deformation of the Mg phase would lead to breakup of the intermetallic layer. It is worth noting that turbulent-like flow features are

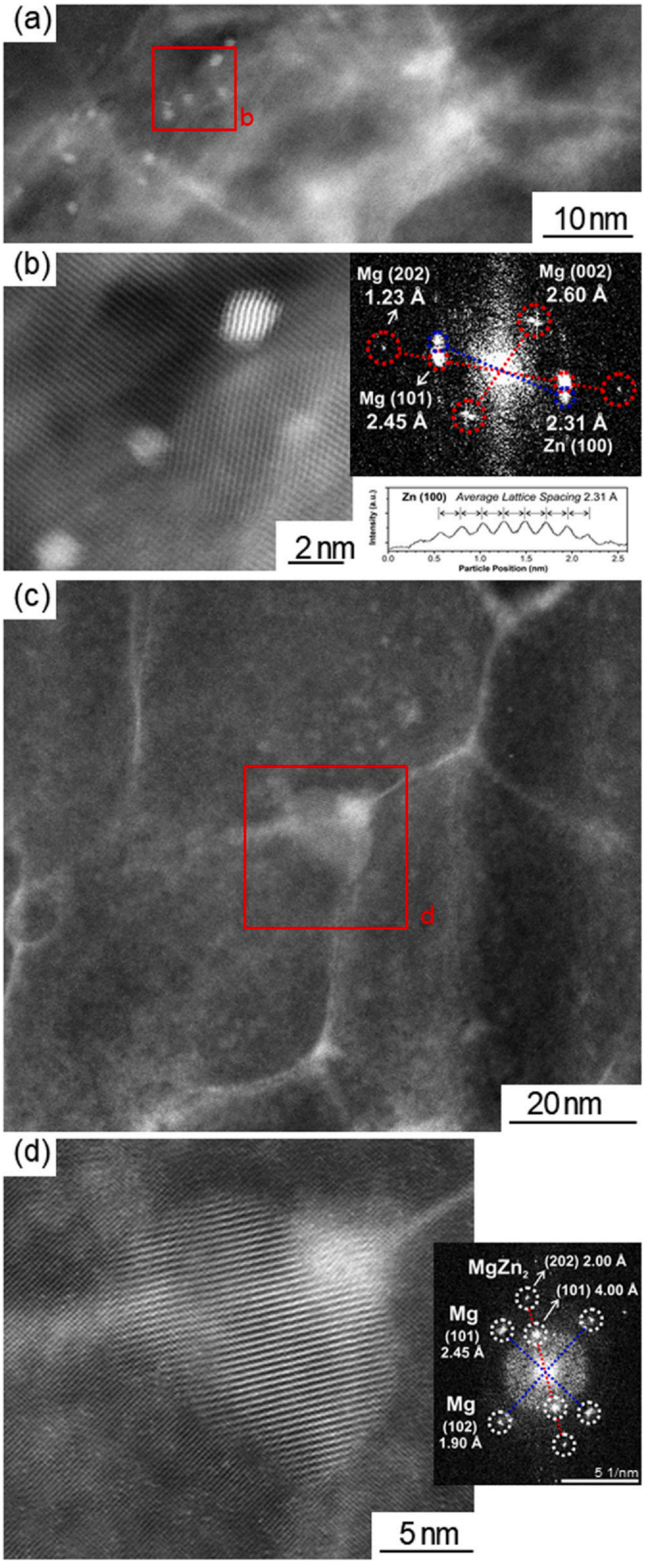

Fig. 9. Mg-20% Zn composite processed to 20 turns of HPT: (a) HAADF-STEM, (b) insert HAADF and respective FFT and HAADF intensity profile, (c) HAADF-STEM of a $MgZn_2$ precipitate at a grain boundary, and (d) insert HAADF and respective FFT.

not readily observed in the Mg-95% Zn composite and such plastic instability of two element under deformation could improve mixing.

In addition to bending, pronounced fragmentation of the Zn phase was observed in the Mg-20% Zn and Mg-50% Zn composites. Careful observation of the area surrounding the Zn particles suggests that mechanical fragmentation takes place at a nanometric scale. It is expected that diffusion assisted dissolution of the Zn phase would lead to a continuous gradient in composition around the Zn particles. However, discrete nanometric volumes of Zn are clearly observed surrounding these particles. The morphology of the Zn particle, and fragments, depicted in Fig. 8(d) resembles the reported finite element simulations of shearing of nonlinear fluids with different viscosities [64]. This supports the assumption that mechanical mixing, rather than atomistic diffusion, plays a major role in mixing Mg and Zn phases.

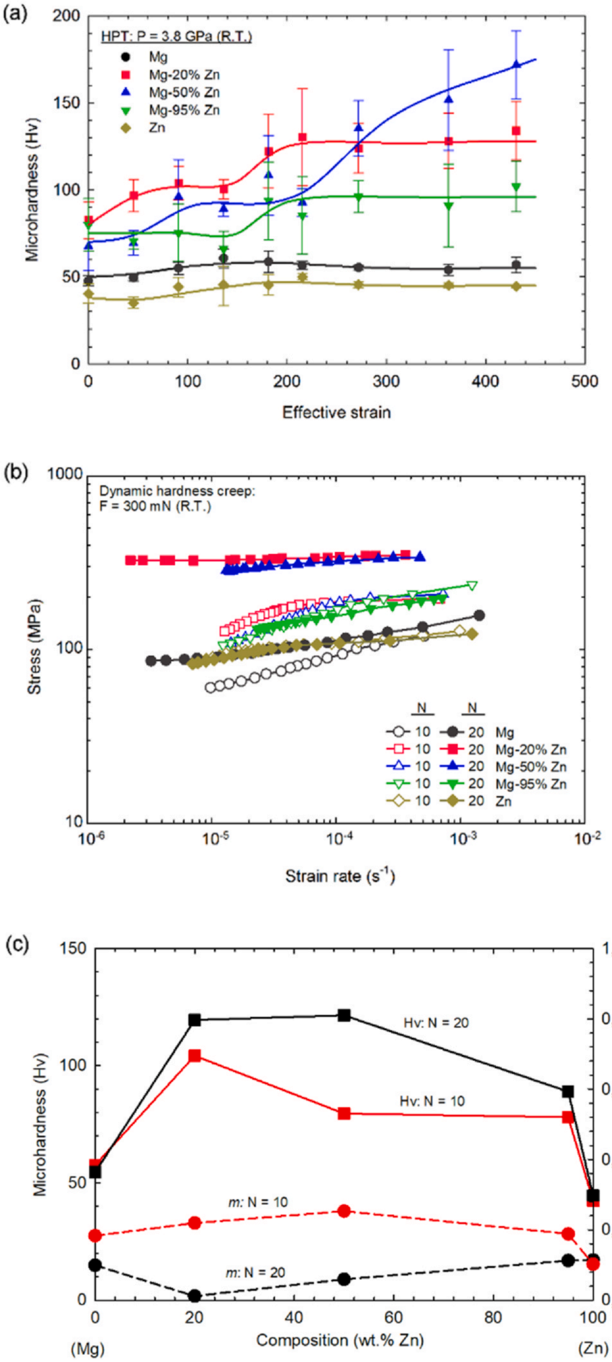

Fig. 10. (a) Vickers microhardness vs effective imposed strain and (b) stress vs. strain rate for the different materials and (c) microhardness and strain-rate sensitivity plotted as a function of the Zn content. (For interpretation of the references to color in this figure, the reader is referred to the web version of this article.)

The small, and sometimes nano-scale, pieces of Zn undergo severe shear leading to the formation of very thin and aligned Zn ribbons in the Mg matrix. The thickness of these ribbons can be so small that they may segregate along Mg grain boundaries as shown in Fig. 8(a). It is important to note that such segregations of Zn were observed throughout the Mg matrix forming a continuous network of segregations. The thick Zn ribbons are aligned along shear direction, but thin segregations of Zn are observed in all orientations implying that diffusion also plays a role in their formation. Thus, the mechanical fragmentation and mixing of phases reduce the distance between Zn particles and therefore facilitate the formation of diffusion-assisted Zn segregations along grain boundaries. Such segregations along grain boundaries act as potential sites for the nucleation of $MgZn_2$ intermetallics.

4.2. Model for structure and mechanical properties evolution

The evolution of hardness with imposed strain shows discrete hardening stages in the composites. These hardening stages reported in systems fabricated by HPT mixing and consolidation of metal powders are attributed to microstructural changes during mixing of phases. Different models of hardness evolution are proposed based on the fraction of each phase and their strength ratio [67]. In the present study, a model for the hardness and structure evolution is presented in Fig. 11 based on microstructural features observed.

Fig. 11(a) illustrates the hardness evolution after HPT process for single phase materials such as pure Mg and pure Zn (black line) and for multi-phase materials such as the Mg-Zn composites (red line). Single phase metallic materials and most alloys display a conventional strain hardening behavior during HPT processing in which the hardness increases at low strains and saturates in a high value [86]. The increase in hardness is associated with grain refinement which is illustrated by sequence (Fig. 11(b) and (c)). The saturation in hardness is associated with a steady structure which remains constant with further deformation. Grain refinement of each phase is also expected at low strains in immiscible systems as the Mg-Zn composites, increasing the overall hardness of the material. This initial grain refinement is illustrated by sequence (Fig. 11(d) and (e)) which shows refined and agglomerated grains forming elongated phases. Further deformation promotes the stretching and fragmentation of the phases and segregations of elements around the phases' interfaces, reducing grain boundary mobility and enabling further grain refinement in the local areas. This is illustrated in Fig. 11(f) which shows grain boundaries without segregations (black lines) and finer grains separated by boundaries with segregations (red lines). Consequently, there is a broad distribution of grain sizes at this stage as observed in the composites processed to 10 turns of HPT. As the fragmentation of phases and segregations are still restricted to some areas, there is no significant increase in hardness. However, further deformation leading to the stretching of the phases reduces the distance between the ribbons, increasing the amount of segregations. This process goes on until the whole sample is affected by the mixing of elements, as illustrated in Fig. 11(g), and this microstructural refinement is associated with a significant increase in hardness. The decrease in overall grain size, the narrowing of the range of grain sizes, fragmentation and thinning of phases and increase in hardness agree with the present observations in the Mg-20% Zn composite processed to 20 turns.

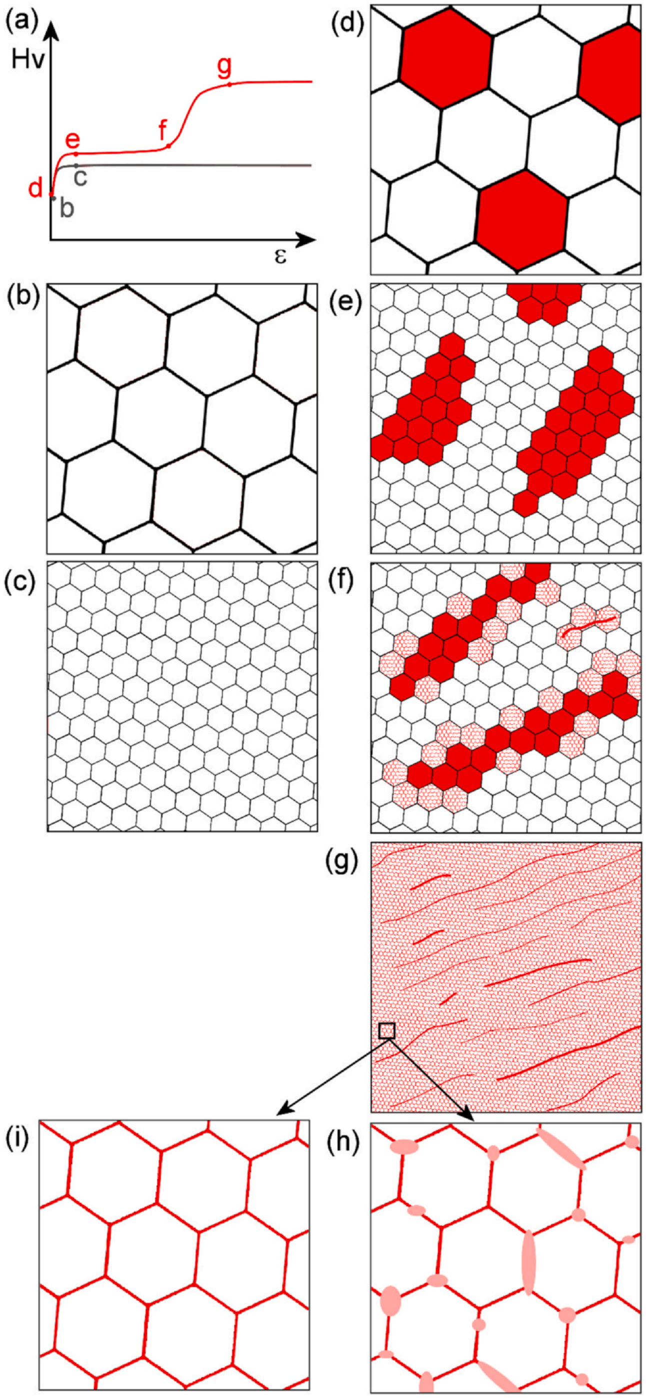

Fig. 11. Model for hardness and microstructure evolution of single-phase materials and multi-phase materials. (For interpretation of the references to color in this figure, the reader is referred to the web version of this article.)

Precipitation of intermetallics is expected in the Mg-Zn system. The pronounced segregations of Zn along Mg grain boundaries convert these boundaries into sites for precipitation of $MgZn_2$ intermetallic. In fact, nanometric precipitates of $MgZn_2$ were observed at Mg grain boundaries in the Mg-20% Zn composite processed by 20 turns of HPT (see Fig. 9). As a consequence, the Zn segregations harden the Mg grain boundaries and prevent grain boundary sliding, which is the deformation mechanism responsible for the inverse Hall-Petch behavior [87] and enhanced strain-rate sensitivity [61] in pure Mg. The tendency for precipitation of intermetallics is illustrated in Fig. 11(h) while segregations of elements that do not precipitate intermetallics is illustrated in Fig. 11(i).

An analysis of data in the literature for different metallic systems processed by SPD suggests that the tendency of formation of intermetallics plays a major role on evolution of strength and strain-rate sensitivity when segregations are developed. For example, HPT mixing of Mg and Al, which tends to form intermetallics, is associated with hardening [25,27,28,88] while HPT processing softened and increased the strain rate sensitivity of a Mg-Li alloy [89], which does not form intermetallics. Also, improved strain-rate sensitivity was reported in an Al-7% Si alloy processed by HPT [90] and the Al-Si system does not display intermetallics. Moreover, it has been shown that HPT processed Zn-Al alloys, which do not form intermetallics, may be softer than the pure components Zn and Al. It has been reported that HPT processing increases the strain-rate sensitivity [91] and may soften [92] a Zn-22% Al alloy. Also, experiments showed that HPT processing of an Al-30% Zn alloy induce formation of Zn segregations along Al grain boundaries which favors the occurrence of grain boundary sliding [93,94], increases strain-rate sensitivity and can introduce superplastic behavior [95]. However, the present experiments show that HPT processing of the Mg-Zn composites induces significant hardening and reduces strain-rate sensitivity after 20 turns despite the introduction of finer grain sizes. Thus, the formation of Zn segregations along grain boundaries, which was associated with improved strain-rate sensitivity in the Al-Zn system [93,94], is associated with increase in strength and decrease in strain-rate sensitivity in the present experiments. The difference in behavior is attributed to the tendency of formation of precipitates in the different systems.

Thus, the present results, which show HPT induced hardening of Mg-Zn composites, agree with other reports of HPT processing of metallic systems associated with intermetallic formation, such as the Mg-Al. The reduced strain-rate sensitivity observed in the Mg-20% Zn and Mg-50% Zn composites processed to 20 turns of HPT is therefore attributed to a Zn segregation hardening of grain boundary areas that prevent grain boundary sliding.

5. Summary and Conclusions

1. Pure Mg and pure Zn particles were mixed in different proportions and consolidated into discs with different compositions using high-pressure torsion. Full consolidation was observed in discs of pure Mg and Mg-20% Zn and Mg-50% Zn composites. Lack of bonding was observed at isolated areas in Mg-95% Zn composite and pure Zn discs.
2. The mixing of phases differs between Mg-rich and Zn-rich composites. Folding, fragmentation and elongation into thin ribbons were observed in the Zn phase in Mg-rich composites. The Mg phase appears less deformed in the Zn-rich composite. $MgZn_2$ intermetallics were formed in all composites but its morphology differs.
3. Mechanical deformation plays a major role in mixing the phases and diffusion contributes to the development of grain boundary segregations. It is shown by the formation of $MgZn_2$ at a Zn segregation along Mg grain boundary.
4. Mg-Zn composites display pronounced hardening and decrease the strain-rate sensitivity with increasing the deformation imposed by HPT. This evolution in mechanical properties differs in the pure Mg and pure Zn observed in the present study and from the reports for the Al-Zn and Mg-Li systems. These effects are attributed to the tendency of formation of intermetallics at segregations at grain boundaries which prevent grain boundary sliding.
5. Discrete hardening stages are observed in the Mg-Zn composites and are attributed to the slow evolution of the microstructure and high amount of strain required to develop segregations. Smaller grain sizes are observed in Mg near areas with significant segregations of Zn.
6. A model is proposed to explain the mixing of phases and its relation to the evolution of mechanical properties.

CRediT authorship contribution statement

Moara M. Castro: Conceptualization, Methodology, Investigation, Writing. **Luciano A. Montoro:** Conceptualization, Methodology, Resources, Writing. **Augusta Isaac:** Conceptualization, Methodology, Resources, Writing. **Megumi Kawasaki:** Conceptualization, Methodology, Resources, Writing. **Roberto B. Figueiredo:** Conceptualization, Methodology, Resources, Writing.

Declaration of Competing Interest

The authors declare that they have no known competing financial interests or personal relationships that could have appeared to influence the work reported in this paper.

Acknowledgements

The authors thank the Microscopy Center of UFMG and the Electron Microscopy Laboratory from LNNano/CNPEM for providing the equipment and technical support during electron microscopy analysis. M.M.C. acknowledges a research fellowship from CAPES. This work was partly supported by CNPq (Grant No. 302445/2018-8), FAPEMIG and CAPES-Proex. This study was partly supported by the National Science Foundation of the United States under Grant No. DMR-1810343 (M.K.).

Appendix A. Supporting information

Supplementary data associated with this article can be found in the online version at doi:10.1016/j.jallcom.2021.159302.

References

[1] I.V. Alexandrov, Y.T. Zhu, T.C. Lowe, R.K. Islamgaliev, R.Z. Valiev, Consolidation of nanometer sized powders using severe plastic torsional straining, Nanostr. Mater. 10 (1) (1998) 45–54.
[2] A.P. Zhilyaev, A.A. Gimazov, G.I. Raab, T.G. Langdon, Using high-pressure torsion for the cold-consolidation of copper chips produced by machining, Mater. Sci. Eng. A 486 (1) (2008) 123–126.
[3] A.R. Yavari, W.J. Botta, C.A.D. Rodrigues, C. Cardoso, R.Z. Valiev, Nanostructured bulk $Al_{90}Fe_5Nd_5$ prepared by cold consolidation of gas atomised powder using severe plastic deformation, Scr. Mater. 46 (10) (2002) 711–716.
[4] W.J. Botta, J.B. Fogagnolo, C.A.D. Rodrigues, C.S. Kiminami, C. Bolfarini, A.R. Yavari, Consolidation of partially amorphous aluminium-alloy powders by severe plastic deformation, Mater. Sci. Eng. A 375–377 (2004) 936–941.
[5] K. Edalati, Y. Yokoyama, Z. Horita, High-pressure torsion of machining chips and bulk discs of amorphous $Zr_{50}Cu_{30}Al_{10}Ni_{10}$, Mater. Trans. 51 (1) (2010) 23–26.
[6] I.V. Alexandrov, R.K. Islamgaliev, R.Z. Valiev, Y.T. Zhu, T.C. Lowe, Microstructures and properties of nanocomposites obtained through SPTS consolidation of powders, Metall. Mater. Trans. A 29 (9) (1998) 2253–2260.
[7] M. Ashida, Z. Horita, T. Kita, A. Kato, Production of Al/Al_2O_3 nanocomposites through consolidation by high-pressure torsion, Mater. Trans. 53 (1) (2012) 13–16.
[8] T. Tokunaga, K. Kaneko, Z. Horita, Production of aluminum-matrix carbon nanotube composite using high pressure torsion, Mater. Sci. Eng. A 490 (1) (2008) 300–304.
[9] T. Tokunaga, K. Kaneko, K. Sato, Z. Horita, Microstructure and mechanical properties of aluminum–fullerene composite fabricated by high pressure torsion, Scr. Mater. 58 (9) (2008) 735–738.
[10] C. Silva, L.A. Montoro, D.A.A. Martins, P.A. Machado, P.H.R. Pereira, B.M. Gonzalez, T.G. Langdon, R.B. Figueiredo, A. Isaac, Interface structures in $Al-Nb_2O_5$ nanocomposites processed by high-pressure torsion at room temperature, Mater. Charact. 162 (2020) 110222.
[11] M.M. Castro, P.H.R. Pereira, A. Isaac, R.B. Figueiredo, T.G. Langdon, Development of a magnesium-alumina composite through cold consolidation of machining chips by high-pressure torsion, J. Alloy. Compd. 780 (2019) 422–427.
[12] M.M. Castro, P.H.R. Pereira, A. Isaac, T.G. Langdon, R.B. Figueiredo, Inverse Hall–Petch behaviour in an AZ91 alloy and in an $AZ91–Al_2O_3$ composite consolidated by high-pressure torsion, Adv. Eng. Mater. 22 (10) (2020) 1900894.
[13] M.M. Castro, W. Wolf, A. Isaac, M. Kawasaki, R.B. Figueiredo, Consolidation of magnesium and magnesium-quasicrystal composites through high-pressure torsion, Lett. Mater. 9 (4) (2019) 546–550.
[14] M.M. Castro, D.R. Lopes, R.B. Soares, D.M.M. dos Santos, E.H.M. Nunes, V.F.C. Lins, P.H.R. Pereira, A. Isaac, T.G. Langdon, R.B. Figueiredo, Magnesium-based bioactive composites processed at room temperature, Materials 12 (16) (2019) 2609.
[15] D. Lopes, R.B. Soares, M.M. Castro, R.B. Figueiredo, T.G. Langdon, V.F.C. Lins, Corrosion behavior in Hank's solution of a magnesium–hydroxyapatite composite processed by high-pressure torsion, Adv. Eng. Mater. 22 (12) (2020) 2000765.
[16] A. Bachmaier, A. Hohenwarter, R. Pippan, New procedure to generate stable nanocrystallites by severe plastic deformation, Scr. Mater. 61 (11) (2009) 1016–1019.

[17] A. Bachmaier, M. Kerber, D. Setman, R. Pippan, The formation of supersaturated solid solutions in Fe–Cu alloys deformed by high-pressure torsion, Acta Mater. 60 (3) (2012) 860–871.

[18] X. Sauvage, P. Jessner, F. Vurpillot, R. Pippan, Nanostructure and properties of a Cu–Cr composite processed by severe plastic deformation, Scr. Mater. 58 (12) (2008) 1125–1128.

[19] X. Sauvage, A. Duchaussoy, G. Zaher, Strain induced segregations in severely deformed materials, Mater. Trans. 60 (7) (2019) 1151–1158.

[20] K. Edalati, R. Uehiro, K. Fujiwara, Y. Ikeda, H.-W. Li, X. Sauvage, R.Z. Valiev, E. Akiba, I. Tanaka, Z. Horita, Ultra-severe plastic deformation: evolution of microstructure phase transformation and hardness in immiscible magnesium-based systems, Mater. Sci. Eng. A 701 (2017) 158–166.

[21] K. Edalati, R. Uehiro, Y. Ikeda, H.-W. Li, H. Emami, Y. Filinchuk, M. Arita, X. Sauvage, I. Tanaka, E. Akiba, Z. Horita, Design and synthesis of a magnesium alloy for room temperature hydrogen storage, Acta Mater. 149 (2018) 88–96.

[22] B. Ahn, H.-J. Lee, I.-C. Choi, M. Kawasaki, J.-I. Jang, T.G. Langdon, Micro-mechanical behavior of an exceptionally strong metal matrix nanocomposite processed by high-pressure torsion, Adv. Eng. Mater. 18 (6) (2016) 1001–1008.

[23] B. Ahn, A.P. Zhilyaev, H.-J. Lee, M. Kawasaki, T.G. Langdon, Rapid synthesis of an extra hard metal matrix nanocomposite at ambient temperature, Mater. Sci. Eng. A 635 (2015) 109–117.

[24] J.-K. Han, H.-J. Lee, J.-I. Jang, M. Kawasaki, T.G. Langdon, Micro-mechanical and tribological properties of aluminum-magnesium nanocomposites processed by high-pressure torsion, Mater. Sci. Eng. A 684 (2017) 318–327.

[25] M. Kawasaki, B. Ahn, H. Lee, A.P. Zhilyaev, T.G. Langdon, Using high-pressure torsion to process an aluminum-magnesium nanocomposite through diffusion bonding, J. Mater. Res. 31 (1) (2016) 88–99.

[26] M. Kawasaki, J.-K. Han, D.-H. Lee, J.-I Jang, T.G. Langdon, Fabrication of nanocomposites through diffusion bonding under high-pressure torsion, J. Mater. Res. 33 (2018) 2700–2710.

[27] M. Kawasaki, J.I. Jang, Micro-mechanical response of an Al-Mg hybrid system synthesized by high-pressure torsion, Materials 10 (6) (2017) 596.

[28] M.M. Castro, S. Sabbaghianrad, P.H.R. Pereira, E.M. Mazzer, A. Isaac, T.G. Langdon, R.B. Figueiredo, A magnesium-aluminium composite produced by high-pressure torsion, J. Alloy. Compd. 804 (2019) 421–426.

[29] J.-K. Han, D.K. Han, G.Y. Liang, J.-I. Jang, T.G. Langdon, M. Kawasaki, Direct bonding of aluminum–copper metals through high-pressure torsion processing, Adv. Eng. Mater. 20 (11) (2018) 1800642.

[30] A. Bachmaier, J. Keckes, K.S. Kormout, R. Pippan, Supersaturation in Ag–Ni alloy by two-step high-pressure torsion processing, Philos. Mag. Lett. 94 (1) (2014) 9–17.

[31] K.S. Kormout, B. Yang, R. Pippan, Deformation behavior and microstructural evolution of Cu–Ag alloys processed by high-pressure torsion, Adv. Eng. Mater. 17 (12) (2015) 1828–1834.

[32] K.S. Kormout, B. Yang, R. Pippan, Transmission electron microscope investigations on Cu-Ag alloys produced by high-pressure torsion, IOP Conf. Ser. Mater. Sci. Eng. 63 (2014) 012092.

[33] K.S. Kormout, P. Ghosh, V. Maier-Kiener, R. Pippan, Deformation mechanisms during severe plastic deformation of a CuAg composite, J. Alloy. Compd. 695 (2017) 2285–2294.

[34] A. Bachmaier, C. Motz, On the remarkable thermal stability of nanocrystalline cobalt via alloying, Mater. Sci. Eng. A 624 (2015) 41–51.

[35] A. Bachmaier, M. Pfaff, M. Stolpe, H. Aboulfadl, C. Motz, Phase separation of a supersaturated nanocrystalline Cu–Co alloy and its influence on thermal stability, Acta Mater. 96 (2015) 269–283.

[36] A. Bachmaier, H. Aboulfadl, M. Pfaff, F. Mücklich, C. Motz, Structural evolution and strain induced mixing in Cu–Co composites studied by transmission electron microscopy and atom probe tomography, Mater. Charact. 100 (2015) 178–191.

[37] A. Bachmaier, J. Schmauch, H. Aboulfadl, A. Verch, C. Motz, On the process of co-deformation and phase dissolution in a hard-soft immiscible CuCo alloy system during high-pressure torsion deformation, Acta Mater. 115 (2016) 333–346.

[38] S.O. Rogachev, S.A. Nikulin, V.M. Khatkevich, R.V. Sundeev, A.A. Komissarov, Features of structure formation in layered metallic materials processed by high pressure torsion, Metall. Mater. Trans. A 51 (4) (2020) 1781–1788.

[39] A. Bachmaier, G.B. Rathmayr, M. Bartosik, D. Apel, Z. Zhang, R. Pippan, New insights on the formation of supersaturated solid solutions in the Cu–Cr system deformed by high-pressure torsion, Acta Mater. 69 (2014) 301–313.

[40] I. Sabirov, R. Pippan, Formation of a W–25%Cu nanocomposite during high pressure torsion, Scr. Mater. 52 (12) (2005) 1293–1298.

[41] I. Sabirov, R. Pippan, Characterization of tungsten fragmentation in a W–25%Cu composite after high-pressure torsion, Mater. Charact. 58 (10) (2007) 848–853.

[42] D. Edwards, I. Sabirov, W. Sigle, R. Pippan, Microstructure and thermostability of a W–Cu nanocomposite produced via high-pressure torsion, Philos. Mag. 92 (33) (2012) 4151–4166.

[43] N. Ibrahim, M. Peterlechner, F. Emeis, M. Wegner, S.V. Divinski, G. Wilde, Mechanical alloying via high-pressure torsion of the immiscible $Cu_{50}Ta_{50}$ system, Mater. Sci. Eng. A 685 (2017) 19–30.

[44] S.O. Rogachev, R.V. Sundeev, D.A. Kozlov, D.V. Khalidova, Structure and hardening of layered steel/copper/steel material subjected to co-deformation by high-pressure torsion, Phys. Met. Metallogr. 120 (2) (2019) 191–196.

[45] S.O. Rogachev, S.A. Nikulin, R.V. Sundeev, Formation of turbulent structures in metallic hybrid materials under pressure torsional deformation, Met. Sci. Heat Treat. 60 (3) (2018) 224–228.

[46] S.O. Rogachev, R.V. Sundeev, V.M. Khatkevich, Evolution of the structure and strength of steel/vanadium alloy/steel hybrid material during severe plastic deformation, Mater. Lett. 173 (2016) 123–126.

[47] S.O. Rogachev, S.A. Nikulin, V.M. Khatkevich, N.Y. Tabachkova, R.V. Sundeev, Structure formation and hardening of the hybrid material based on vanadium and zirconium alloys during high-pressure torsion, Russ. Metall. 2018 (4) (2018) 372–376.

[48] D. Luo, T. Huminiuc, Y. Huang, T. Polcar, T.G. Langdon, The fabrication of high strength Zr/Nb nanocomposites using high-pressure torsion, Mater. Sci. Eng. A 790 (2020) 139693.

[49] D. Hernández-Escobar, R.R. Unocic, M. Kawasaki, C.J. Boehlert, High-pressure torsion processing of Zn–3Mg alloy and its hybrid counterpart: a comparative study, J. Alloy. Compd. 831 (2020) 154891.

[50] D. Hernández-Escobar, J. Marcus, J.-K. Han, R.R. Unocic, M. Kawasaki, C.J. Boehlert, Effect of post-deformation annealing on the microstructure and micro-mechanical behavior of Zn–Mg hybrids processed by high-pressure torsion, Mater. Sci. Eng. A 771 (2020) 138578.

[51] D. Hernández-Escobar, Z.U. Rahman, H. Yilmazer, M. Kawasaki, C.J. Boehlert, Microstructural evolution and intermetallic formation in Zn-Mg hybrids processed by high-pressure torsion, Philos. Mag. 99 (5) (2019) 557–584.

[52] J. Kubásek, D. Vojtěch, E. Jablonská, I. Pospíšilová, J. Lipov, T. Ruml, Structure, mechanical characteristics and in vitro degradation, cytotoxicity, genotoxicity and mutagenicity of novel biodegradable Zn–Mg alloys, Mater. Sci. Eng. C 58 (2016) 24–35.

[53] C.L.P. Silva, A.C. Oliveira, C.G.F. Costa, R.B. Figueiredo, M. de Fátima Leite, M.M. Pereira, V.F.C. Lins, T.G. Langdon, Effect of severe plastic deformation on the biocompatibility and corrosion rate of pure magnesium, J. Mater. Sci. 52 (10) (2017) 5992–6003.

[54] C.L.P. Silva, R.B. Soares, P.H.R. Pereira, R.B. Figueiredo, V.F.C. Lins, T.G. Langdon, The effect of high-pressure torsion on microstructure, hardness and corrosion behavior for pure magnesium and different magnesium alloys, Adv. Eng. Mater. 21 (3) (2019) 1801081.

[55] D.R. Lopes, C.L.P. Silva, R.B. Soares, P.H.R. Pereira, A.C. Oliveira, R.B. Figueiredo, T.G. Langdon, V.F.C. Lins, Cytotoxicity and corrosion behavior of magnesium and magnesium alloys in Hank's solution after processing by high-pressure torsion, Adv. Eng. Mater. 21 (8) (2019) 1900391.

[56] B. Srinivasarao, A.P. Zhilyaev, T.G. Langdon, M.T. Pérez-Prado, On the relation between the microstructure and the mechanical behavior of pure Zn processed by high pressure torsion, Mater. Sci. Eng. A 562 (2013) 196–202.

[57] R.B. Figueiredo, T.G. Langdon, Processing magnesium and its alloys by high-pressure torsion: an overview, Adv. Eng. Mater. 21 (1) (2019) 1801039.

[58] S. Liu, D. Kent, N. Doan, M. Dargusch, G. Wang, Effects of deformation twinning on the mechanical properties of biodegradable Zn-Mg alloys, Bioact. Mater. 4 (2019) 8–16.

[59] A. Jarzębska, M. Bieda, J. Kawałko, Ł. Rogal, P. Koprowski, K. Sztwiertnia, W. Pachla, M. Kulczyk, A new approach to plastic deformation of biodegradable zinc alloy with magnesium and its effect on microstructure and mechanical properties, Mater. Lett. 211 (2018) 58–61.

[60] H. Somekawa, T. Mukai, Effect of grain boundary structures on grain boundary sliding in magnesium, Mater. Lett. 76 (2012) 32–35.

[61] R.B. Figueiredo, S. Sabbaghianrad, A. Giwa, J.R. Greer, T.G. Langdon, Evidence for exceptional low temperature ductility in polycrystalline magnesium processed by severe plastic deformation, Acta Mater. 122 (2017) 322–331.

[62] P. Zhang, S.X. Li, Z.F. Zhang, General relationship between strength and hardness, Mater. Sci. Eng. A 529 (2011) 62–73.

[63] A.P. Zhilyaev, T.G. Langdon, Using high-pressure torsion for metal processing: fundamentals and applications, Prog. Mater. Sci. 53 (6) (2008) 893–979.

[64] M. Pouryazdan, B.J.P. Kaus, A. Rack, A. Ershov, H. Hahn, Mixing instabilities during shearing of metals, Nat. Commun. 8 (1) (2017) 1611.

[65] K.S. Kormout, R. Pippan, A. Bachmaier, Deformation-induced supersaturation in immiscible material systems during high-pressure torsion, Adv. Eng. Mater. 19 (4) (2017) 1600675.

[66] C.L.P. Silva, I.C. Tristão, S. Sabbaghianrad, S.A. Torbati-Sarraf, R.B. Figueiredo, T.G. Langdon, Microstructure and hardness evolution in magnesium processed by HPT, Mater. Res. 20 (2017) 2–7.

[67] K.S. Kormout, R. Pippan, A. Bachmaier, Deformation-induced supersaturation in immiscible material systems during high-pressure torsion, Adv. Eng. Mater. 19 (4) (2017) 1600675.

[68] R.B. Figueiredo, F.S.J. Poggiali, C.L.P. Silva, P.R. Cetlin, T.G. Langdon, The influence of grain size and strain rate on the mechanical behavior of pure magnesium, J. Mater. Sci. 51 (6) (2016) 3013–3024.

[69] R.H. Wagoner, Strain-rate sensitivity of zinc sheet, Metall. Mater. Trans. A 15 (6) (1984) 1265–1271.

[70] Y.Z. Tian, S.D. Wu, Z.F. Zhang, R.B. Figueiredo, N. Gao, T.G. Langdon, Microstructural evolution and mechanical properties of a two-phase Cu-Ag alloy processed by high-pressure torsion to ultrahigh strains, Acta Mater. 59 (7) (2011) 2783–2796.

[71] A. Hohenwarter, A. Taylor, R. Stock, R. Pippan, Effect of large shear deformations on the fracture behavior of a fully pearlitic steel, Metall. Mater. Trans. A 42 (6) (2011) 1609–1618.

[72] Y. Huang, M. Kawasaki, T.G. Langdon, Influence of anvil alignment on shearing patterns in high-pressure torsion, Adv. Eng. Mater. 15 (8) (2013) 747–755.

[73] Y. Huang, M. Kawasaki, T.G. Langdon, An investigation of flow patterns and hardness distributions using different anvil alignments in high-pressure torsion, J. Mater. Sci. 48 (13) (2013) 4533–4542.

[74] Y. Huang, M. Kawasaki, T.G. Langdon, An evaluation of the shearing patterns introduced by different anvil alignments in high-pressure torsion, J. Mater. Sci. 49 (8) (2014) 3146–3157.
[75] R.B. Figueiredo, G.C.V. De Faria, P.R. Cetlin, T.G. Langdon, Three-dimensional analysis of plastic flow during high-pressure torsion, J. Mater. Sci. 48 (13) (2013) 4524–4532.
[76] A. Gola, R. Schwaiger, P. Gumbsch, L. Pastewka, Pattern formation during deformation of metallic nanolaminates, Phys. Rev. Mater. 4 (1) (2020) 013603.
[77] Y. Beygelzimer, Vortices and mixing in metals during severe plastic deformation, Mater. Sci. Forum 683 (2011) 213–224.
[78] R. Kulagin, Y. Beygelzimer, Y. Ivanisenko, A. Mazilkin, B. Straumal, H. Hahn, Instabilities of interfaces between dissimilar metals induced by high pressure torsion, Mater. Lett. 222 (2018) 172–175.
[79] R. Kulagin, Y. Zhao, Y. Beygelzimer, L.S. Toth, M. Shtern, Modeling strain and density distributions during high-pressure torsion of pre-compacted powder materials, Mater. Res. Lett. 5 (3) (2017) 179–186.
[80] R. Kulagin, Y. Beygelzimer, Y. Ivanisenko, A. Mazilkin, H. Hahn, High pressure torsion: from laminar flow to turbulence, IOP Conf. Ser. Mater. Sci. Eng. 194 (2017) 012045.
[81] A. Hohenwarter, A. Bachmaier, B. Gludovatz, S. Scheriau, R. Pippan, Technical parameters affecting grain refinement by high pressure torsion, Int. J. Mater. Res. 100 (12) (2009) 1653–1661.
[82] R.B. Figueiredo, M.T.P. Aguilar, P.R. Cetlin, T.G. Langdon, Deformation heterogeneity on the cross-sectional planes of a magnesium alloy processed by high-pressure torsion, Metall. Mater. Trans. A 42 (10) (2011) 3013–3021.
[83] R.B. Figueiredo, T.G. Langdon, Development of structural heterogeneities in a magnesium alloy processed by high-pressure torsion, Mater. Sci. Eng. A 528 (13–14) (2011) 4500–4506.
[84] Y. Cao, Y.B. Wang, R.B. Figueiredo, L. Chang, X.Z. Liao, M. Kawasaki, W.L. Zheng, S.P. Ringer, T.G. Langdon, Y.T. Zhu, Three-dimensional shear-strain patterns induced by high-pressure torsion and their impact on hardness evolution, Acta Mater. 59 (10) (2011) 3903–3914.
[85] Y.Z. Tian, X.H. An, S.D. Wu, Z.F. Zhang, R.B. Figueiredo, N. Gao, T.G. Langdon, Direct observations of microstructural evolution in a two-phase Cu-Ag alloy processed by high-pressure torsion, Scr. Mater. 63 (1) (2010) 65–68.
[86] M. Kawasaki, T. Langdon, Review: achieving superplasticity in metals processed by high-pressure torsion, J. Mater. Sci. 49 (19) (2014) 6487–6496.
[87] H. Somekawa, T. Mukai, Hall–Petch breakdown in fine-grained pure magnesium at low strain rates, Metall. Mater. Trans. A 46 (2) (2015) 894–902.
[88] M. Kawasaki, B. Ahn, H. Lee, A.P. Zhilyaev, T.G. Langdon, Using high-pressure torsion to process an aluminum–magnesium nanocomposite through diffusion bonding, J. Mater. Res. 31 (1) (2015) 88–99.
[89] K. Edalati, T. Masuda, M. Arita, M. Furui, X. Sauvage, Z. Horita, R.Z. Valiev, Room-temperature superplasticity in an ultrafine-grained magnesium alloy, Sci. Rep. 7 (2017) 2662.
[90] P. Kumar, M. Kawasaki, T.G. Langdon, Review: overcoming the paradox of strength and ductility in ultrafine-grained materials at low temperatures, J. Mater. Sci. 51 (1) (2016) 7–18.
[91] M. Kawasaki, H.-J. Lee, I.-C. Choi, J.-I Jang, B. Ahn, T.G. Langdon, Evolution of hardness, microstructure, and strain rate sensitivity in a Zn-22% Al eutectoid alloy processed by high-pressure torsion, IOP Conf. Ser. Mater. Sci. Eng. 63 (2014) 012101.
[92] M. Kawasaki, B. Ahn, T.G. Langdon, Microstructural evolution in a two-phase alloy processed by high-pressure torsion, Acta Mater. 58 (3) (2010) 919–930.
[93] N.Q. Chinh, R.Z. Valiev, X. Sauvage, G. Varga, K. Havancsák, M. Kawasaki, B.B. Straumal, T.G. Langdon, Grain boundary phenomena in an ultrafine-grained Al–Zn alloy with improved mechanical behavior for micro-devices, Adv. Eng. Mater. 16 (8) (2014) 1000–1009.
[94] N.Q. Chinh, T. Csanádi, T. Győri, R.Z. Valiev, B.B. Straumal, M. Kawasaki, T.G. Langdon, Strain rate sensitivity studies in an ultrafine-grained Al–30wt% Zn alloy using micro- and nanoindentation, Mater. Sci. Eng.: A 543 (2012) 117–120.
[95] K. Edalati, Z. Horita, R.Z. Valiev, Transition from poor ductility to room-temperature superplasticity in a nanostructured aluminum alloy, Sci. Rep. 8 (1) (2018) 6740.